

A mixed phase-field fracture model for crack propagation in punctured EPDM strips

Katrin Mang^{1,*}, Andreas Fehse², Nils Hendrik Kröger^{2,3}, Thomas Wick¹

¹Institute of Applied Mathematics, Leibniz Universität Hannover, Welfengarten 1, 30167 Hannover, Germany

²Deutsches Institut für Kautschuktechnologie e. V., Eupener Straße 33, 30519 Hannover, Germany

³material prediction GmbH, Nordkamp 14, 26203 Wardenburg, Germany

January 7, 2022

Abstract

In this work, we present crack propagation experiments evaluated by digital image correlation (DIC) for a carbon black filled ethylene propylene diene monomer rubber (EPDM) and numerical modeling with the help of variational phase-field fracture. Our main focus is the evolution of cracks in one-sided notched EPDM strips containing a circular hole. The crack propagation experiments are complemented with investigations identifying the mechanical material properties as well as the critical strain energy release rate. For simulating the evolution of cracks with a given notch, phase-field fracture modeling is a popular approach. To avoid volume-locking effects considering fractures in nearly incompressible materials, a quasi-static phase-field fracture model in its classical formulation is reformulated with the help of a mixed form of the solid-displacement equation. The new established mixed phase-field fracture model is applied to simulate crack propagation in punctured EPDM strips by using the experimentally identified material parameters with mixed finite elements. To discuss agreements and point out challenges and differences, the crack paths, the maximal force response, the traverse displacement at the crack start, as well as force-displacement curves of the experimental and numerical results are compared.

Keywords— EPDM rubber, Fatigue testing, Material Characterization, Incompressibility, Mixed finite elements, Phase-field fracture

1 Introduction

In the recent past, many authors contributed to improve the understanding of the fatigue behavior of elastomeric materials. Applied fatigue models often concentrate on the end-of-life behaviour, e.g. by Wöhler's method, e.g. [1, 2]. Later approaches combine the classic Paris-Erdogan approach for crack propagation with statistical particle distribution and particle size distribution, e.g. [3, 4, 5]. Another alternative is the continuum damage mechanics approach, e.g. [6, 7]. A challenging task within modeling fatigue is the correct prediction of the crack propagation via finite element simulations. Classical approaches to simulate the growth of a crack are based on energetic failure criteria using the virtual crack extension method [8] or crack tip closure method [8, 9]. Similar approaches consider cohesive elements, see e.g. [10] for an application using inelastic cohesive models.

In mechanics, phase-field models for quasi-static brittle fracture based on Griffith's theory [11] are a well-established approach to simulate complex crack phenomena as crack nucleation, propagation, branching or merging. Phase-field modeling is based on a smoothed indicator variable called crack phase-field parameter describing a fracture path continuously over the displacement field. A first variational approach for quasi-static brittle fracture was introduced by Francfort and Marigo [12], see also [13]. A regularized formulation was presented two years later by Bourdin et al. [14]. This formulation is motivated by the regularization of Ambrosio and Tortorelli [15] for elliptic free-discontinuity problems. Often in the literature, the Ambrosio-Tortorelli functional with a quadratic energy degradation function (AT₂) is considered in the context of phase-field fracture problems. To decrease the impact of a possibly material-dependent length scale parameter ϵ , Wu [16, 17, 18] introduced a unified phase-field theory with the idea that the unknown phase-field and its gradient are introduced to regularize the sharp crack topology in a purely geometric context. See [16] for a

*Corresponding author: mang@ifam.uni-hannover.de

detailed description. Furthermore, Amor et al. [19] proposed a volumetric-deviatoric decomposition of the elastic energy density, because the regularized formulation does not distinguish between fracture behaviour in tension and compression [20]. Detailed overviews on phase-field fracture modeling from mechanical and mathematical perspectives are given by Ambati et al. [20], Wu et al. [21], Bourdin and Francfort [22], and Wick [23].

If the considered solid is nearly incompressible, e.g. EPDM, the classical Euler-Lagrange equations derived from a regularized energy functional fail due to volume locking effects. Locking in finite element simulations leads to the problem, that the solid displacements are underestimated and unrealistic numerical results can be observed. To allow also simulating crack growth in rubber-like materials, the phase-field fracture model is extended, see [24, 25] for a detailed derivation. This approach builds on a mixed form of the solid-displacement equation resulting in two unknowns: a displacement field and a pressure variable. Via Taylor-Hood elements we achieve a stable discretization of the displacement-pressure system. Alternative approaches have been presented by Loew et al. [26, 27] for rate-dependent phase field damage models or by Faye et al. [28] for mass sink models based on [29].

In this work, the mixed phase-field fracture model is tested on punctured EPDM strips with a notch on one side, which are stretched until total failure. Being well aware of geometric and material non-linearities dealing with rubber and high strains, in this contribution we neglect those effects focusing on the modeling approach as well as on the qualitative comparison to the experiments. Whereas the experiments themselves are a benchmark for future studies. In addition, it is sufficient to assume plane-stress since the experimental specimens are thin and for this reason, two-dimensional numerical simulations are justified. With these simplifications we cannot expect perfect matches between numerical simulations and experiments. However, due to the complexity of the experimental setup and our newly developed mixed phase-field fracture model using Wu’s functional, such qualitative comparisons are a major effort.

To this end, the main contributions and the outline of this work are:

- Determining the material compounding and properties as well as the (critical) strain energy release rate via digital image correlation (DIC) in Section 2.1 and 2.2;
- Deriving a quasi-static mixed phase-field fracture model based on Wu’s model [16] and Amor’s strain energy splitting [19] for incompressible solids similar to [24], in Section 3.1 and 3.2;
- Applying and substantiating the new model via numerical simulations of crack propagation in punctured EPDM strips in Section 4 and discussions in Section 5.

Section 6 summarizes the content and the main results of this work.

2 Experiments - mechanical characterization and crack path analysis

2.1 Material compounding and sample preparation

The experimental study is conducted using a sulphur crosslinked EPDM (Keltan 2450) filled with 60 phr carbon black N550. The EPDM mixture, see Table 1, is prepared on a 5.0 liter mixer adding the ingredients step-wise. The crosslinking agent and catalysts are admixed at a roller at 60°C. The samples, 2mm thick specimens for all experiments, are compression moulded at 170°C for six minutes corresponding to “ t_{90} ” plus two minutes of an according vulcameter test¹. If required for the experiments, notches and circular inclusions are pierced in the specimens after vulcanisation.

Ingredients	EPDM	Carbon black N550	PEG- 4000	Oil	Zinc oxid	Stearic acid	Sulphur	TBBS	TBzTD
Phr	100	60	5.0	5.0	5.0	3.0	0.7	1.0	3.5
Admixed at	Mixer						Roller		
Admixed after min	0	2/3@1 1/3@2	2m30	1	2m30	1	1	1	1

Table 1: Recipe of the investigated EPDM mixture (phr $\hat{=}$ parts per hundred parts of rubber related to mass parts).

¹ “ t_{90} ” denotes the time where the torque of the vulcameter curve reaches 90% of its maximum.

2.2 Determination of mechanical material properties

Elastic constants. The mechanical material properties are determined on a ZWICK Universal test machine in four loading modes - uniaxial, planar (pure shear) and biaxial tension as well as confined (volumetric) compression. The tests were conducted with a (initial) strain rate of approximately 50% per minute and a pre-force of 1N, cf. Figure 1 (black line). The later defined material model uses a linear elastic approach such that the minor non-linear behaviour has to be estimated by e.g. the average behaviour until a certain strain, a lower or upper bound or alternative with an estimate for the Young's modulus in consistency with the Neo Hooke model (estimate holds for the initial stiffness, therefore one possibility for an upper bound definition), see Figure 1 (gray line for 'up to 150% estimate' and green line for 'Neo Hooke estimate'). The bulk modulus is derived by volumetric compression experiments within the constant response region of 1000 to 2000N, see Figure 2. The parameter identification is done by using a minimization for the least square sum of the absolute errors between experiment and prediction considering the varying strain range. The resulting parameters are depicted in Tabular 2. The estimation of linear material behavior might deviate for strains under 50% but is a solid assumption for higher strains appearing in the later crack path experiments for this special EPDM.

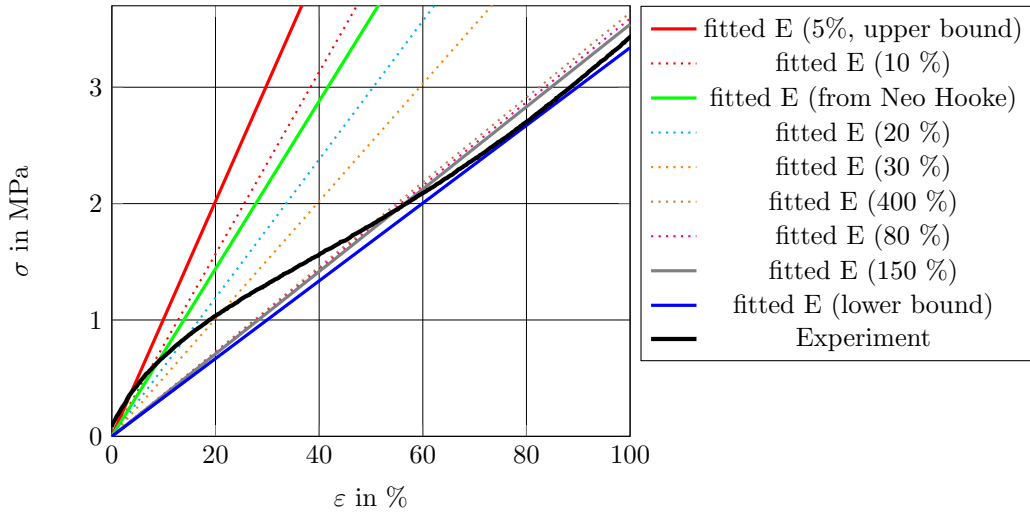


Figure 1: Uniaxial tension test (stress σ versus strain ε) and prediction of the elastic behaviour based on parameter identifications of the elastic moduli related to specific fitting strain ranges.

Parameter	upper	Neo Hooke	10	20	80	150	400	lower
E [MPa]	10.1	7.20	7.83	5.95	3.59	3.54	3.64	3.34
K [MPa]	2595	2595	2595	2595	2595	2595	2595	2595
λ [MPa]	2592.75	2593.40	2593.26	2593.68	2594.20	2594.21	2594.19	2594.26
μ [MPa]	3.37	2.40	2.61	1.98	1.20	1.18	1.21	1.11
ν []	0.49978	0.49985	0.49983	0.49987	0.49992	0.49992	0.49992	0.49993

Table 2: Young's modulus E , bulk modulus K , Lamé coefficients λ and μ and Poisson ratio ν for different identification variants of E (upper and lower bound, resp. results for parameter fit up to $X\%$ of strain, and estimated by Neo Hookean model), cf. Figures 1 and 2. Parameters set in light blue are used in the simulations in Section 4.

Critical energy release rate. Pure shear tests were used to determine the (critical) energy release rate G_c . The specimens had a length of 196mm, a height of 28mm and a thickness of 1.8mm. A ZWICK 1445 universal test machine was used for the tests. The traverse velocity was chosen to be 200mm/min. Two types of tests were conducted: standard pure shear tests until break, and pure shear tests with notched samples. The notched sample had an initial crack c_0 of 47mm. In the second case, a square pattern was applied to the specimen such that the crack growth could be followed by a DIC recording. The crack growth was correlated with the recorded force-displacement curves. The resulting force-displacement and crack growth curves are shown in Figure 3. The critical (strain) energy release rate can be determined using this data and the following formula from [32, 33]:

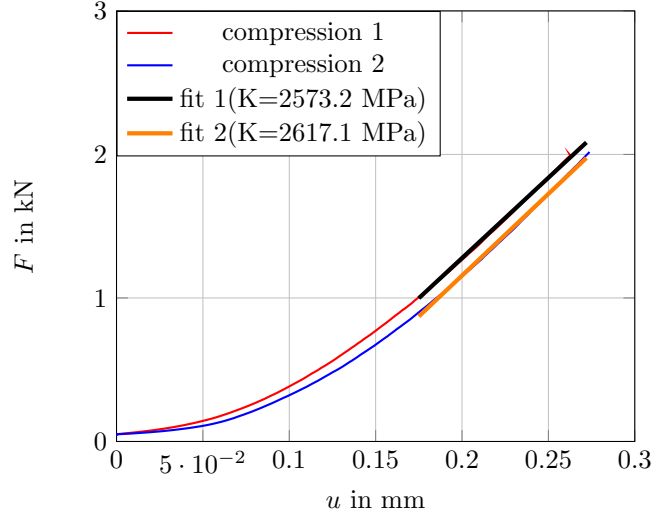


Figure 2: Volumetric compression test and estimation of the bulk modulus by a linear fit in the range between 1 and 2kN. The force F and displacement u are depicted in sense of compression, compared to tension the sign would switch. Please refer to [30, 31] for details on the experimental setup.

$$G_c = - \left. \frac{\partial U}{\partial A} \right|_{\lambda} = - \left. \frac{dU}{dA} \right|_{\lambda}.$$

Here, U is the stored elastic energy and dU is the difference between the sample with and without a crack, [32, 33]. With F_w and u_w being the force-displacement data of the sample without a crack, F_c and u_c being the data of the sample with a crack, and λ as the stretch, dU reads as

$$dU = \int_{\lambda} F_w du_w - \int_{\lambda} F_c du_c.$$

The crack area dA depends on the specimen thickness t and the crack length $c_0 + c$. Here, c_0 is the initial crack length of 47mm and c is the length of the growing crack, cf. [32, 33]:

$$dA = (c_0 + c) \cdot t.$$

Evaluating the experimental results the stationary value of the critical strain energy release rate G_c can be approximated by 17.0N/mm, see Figure 4. The result coincides in general with literature results, see e.g. [34] for carbon black filled styrene butadiene rubber.

2.3 Crack path experiments

In order to investigate the crack path behavior, punctured strips are elongated with 200mm/min (related to traverse velocity) in a ZWICK Universal test machine till total failure. An inhomogeneous forming strain and stress field during the experiment is introduced by a circular hole of 8mm diameter in the upper right part of the strip, cf. Figure 10. A similar experimental setup was proposed and investigated in [35]. Variations of the experiments are realized by varying the position of the given notch on the left side with a length of 1mm at 6, 10, 12, 14 and 18mm height (from the bottom boundary). In all experiments the hole has a high influence on the crack path. For an initial position from 6 to 10mm the crack path is diverted towards the hole. While for 6 and 10mm the crack propagates below the hole towards the right edge, for 12, 14 and 18mm the crack is stopped for a short time by the hole, propagating afterwards nearly at the middle right inner edge of the hole towards the boundary edge of the specimen, see Figures 5 and 6. Comparing the start of the propagating fracture, the notch height only has minor influence on the force response. Although the distance between the initial notch and the circular hole is the shortest for the 14mm test, the resistance is quite strong. A clear trend between initial notch position and the start of the force drop in terms of the global displacement is not observable, cf. Figure 9. The high deviation in the (starting) crack behaviour between same experiments is typical for

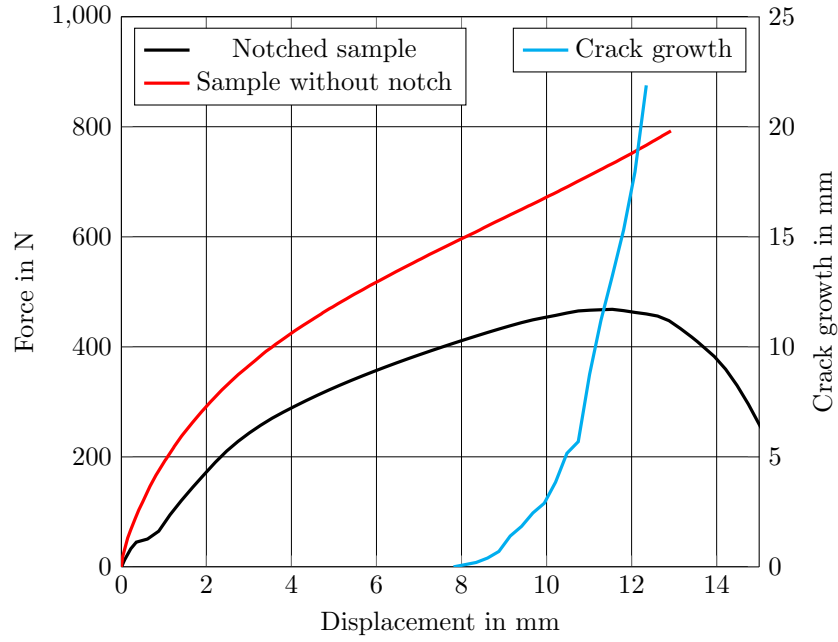


Figure 3: Force-displacement curves (displacement u in y -direction measured on the top boundary versus force F_y) for a notched sample and a sample without notch. Further, the crack growth evaluated from DIC, cf. Figure 4, in dependence of the displacement is plotted in blue.

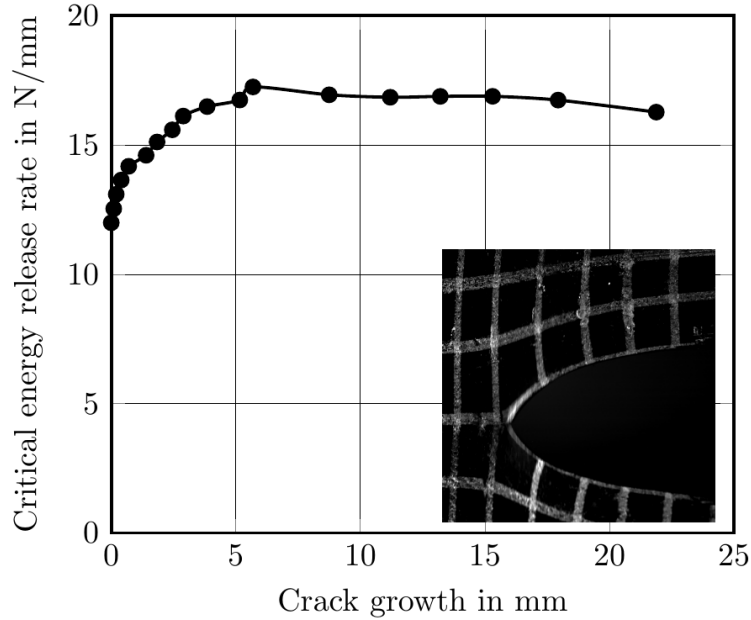


Figure 4: Estimated (critical) strain energy release rate G_c in dependence of the crack length of a single-edge notched pure shear tension test. The average value in the stable crack growth region after 5.0mm crack length is approximately 17.0N/mm.

carbon black filled rubbers. Despite the deviations in the force drop, the crack path is quite stable within the group of same experiments for one notch height, cf. Figure 6.

In Figure 8, the maximal loading forces at the crack start are given for the experiments on punctured strips with different notch height compared to the numerical results for each test. Concerning the experiments one can see a fully evolved crack to the opposite edge (6 and 10mm) respectively or an evolved crack to the hole (12, 14 and 18mm), cf. Figures 5, 6 and 7. In red (left bar) and blue (right bar) in Figure 8, the numerical results for the force maximum are plotted, based on the two coloured parameter settings from Table 2 for the notch heights of 6 to 18mm.

In Figure 9, the experimental and numerical results of the traverse displacement at the first force maximum from Figure 8 are presented. The grey bars in the middle give the experimental weighted results including natural scattering of the experiments. In red (left bar) and blue (right bar), the results for the maximal displacement at the force maximum are plotted based on the parameter settings from Table 2.

3 A quasi-static phase-field model for nearly incompressible solids

In this section, a quasi-static phase-field fracture model is proposed which is used to simulate crack propagation of the experiments described in the previous Section 2. In the following, the used mixed phase-field fracture model is given as well as a description on the numerical solving and the implementation of the finite element simulation, see Section 3.3. In Section 4, the numerical results concerning the punctured EPDM strips are presented and compared to the experimental results considering the crack paths and force-displacement curves.

3.1 Notation, spaces and preliminaries

In the following, we emanate from a two-dimensional, open and smooth domain $\Omega \subset \mathbb{R}^2$ where Γ_D denotes the Dirichlet boundary. Let \mathcal{I} be a loading interval $[0, T]$, where $T > 0$ is the end time value. A displacement function u is given as $u : (\Omega \times \mathcal{I}) \rightarrow \mathbb{R}^2$. Further, a smooth indicator function $\varphi : (\Omega \times \mathcal{I}) \rightarrow [0, 1]$ is named phase-field function with $\varphi = 0$ in the broken, and $\varphi = 1$ in the unbroken material. The physics of the underlying problem ask to enforce crack irreversibility, i.e., that φ is monotone non-increasing with respect to $t \in \mathcal{I}$.

By $(a, b) := \int_{\Omega} a \cdot b \, dx$ for vectors a, b , the L^2 scalar-product is denoted. The Frobenius scalar product of two matrices of the same dimension is defined as $(A : B) := \sum_i \sum_j a_{ij} b_{ij}$ and therewith the L^2 -scalar product is given by $(A, B) := \int_{\Omega} A : B \, dx$.

To allow for a weak problem formulation, we consider a subdivision $0 = t_0 < t_1 < \dots < t_N = T$ of the interval \mathcal{I} . In each time step, we define approximations $(u^n, \varphi^n) \approx (u(t_n), \varphi(t_n))$ and hence the irreversibility condition is approximated by $\varphi^n \leq \varphi^{n-1}$ for all $n = 1, \dots, N$. The phase-field space is $\mathcal{W} := H^1(\Omega)$ with a convex subset $\mathcal{K} := \{\psi \in \mathcal{W} \mid \psi \leq \varphi^{n-1} \leq 1\}$. Further, we define the function spaces $\mathcal{V} := (H_0^1(\Omega))^2 := \{w \in (H^1(\Omega))^2 \mid w = 0 \text{ a.e. on } \Gamma_D\}$ and $\mathcal{U} := L_2(\Omega)$.

In the following, the critical energy release rate is denoted by G_c . To guarantee well-conditioning of the system of equations, a degradation function is defined as $g(\varphi) := (1 - \kappa)\varphi^2 + \kappa$, with a small regularization parameter $\kappa > 0$. The stress tensor $\sigma(u)$ is given by $\sigma(u) := 2\mu E_{\text{lin}}(u) + \lambda \text{tr}(E_{\text{lin}}(u))\mathbf{I}$ with the Lamé coefficients $\mu, \lambda > 0$. The linearized strain tensor therein is defined as $E_{\text{lin}}(u) := \frac{1}{2}(\nabla u + \nabla u^T)$. By \mathbf{I} , the two-dimensional identity matrix is denoted.

We follow Wu [16] for a unified phase-field fracture model with the energy functional

$$E_{\epsilon}(u, \varphi) = \int_{\Omega} \frac{g(\varphi)}{2} \sigma(u) : E_{\text{lin}}(u) \, dx + \int_{\Omega} \frac{G_c}{\pi} \frac{2(1 - \varphi) - (1 - \varphi)^2}{\epsilon} \, dx + \int_{\Omega} \frac{G_c}{\pi} \epsilon |\nabla \varphi|^2 \, dx, \quad (1)$$

where $\epsilon > 0$ is the usual phase-field regularization parameter, describing the bandwidth of the transition zone between broken and unbroken material.

Remark 1 (Wu's energy functional) *Ambrosio and Tortorelli [15, 36] proposed an elegant way to approximate the Mumford-Shah functional [37] for image segmentation by an elliptic functional defined on Sobolev spaces. The key idea was to replace the sharp lower-dimensional crack by a smoothed indicator function while Γ -convergence to the Mumford-Shah functional is guaranteed for a length scale $\epsilon \rightarrow 0$. This in turn satisfies Griffith's law of crack propagation. Simultaneously, Bourdin et al. [14] proposed a regularized energy functional for brittle fracture. The so called AT_2 functional (named as in [38]) is defined as*

$$AT_2 : \quad E_{\epsilon}(u, \varphi) = \int_{\Omega} \frac{g(\varphi)}{2} \sigma(u) : E_{\text{lin}}(u) \, dx + \int_{\Omega} \frac{G_c}{2} \frac{(1 - \varphi)^2}{\epsilon} \, dx + \int_{\Omega} \frac{G_c}{2} \epsilon |\nabla \varphi|^2 \, dx. \quad (2)$$



Figure 5: Overview of the executed tests concerning tracking of the crack paths, back side of tested punctured strips, with an initially given notch of 1mm length and 18, 14, 12, 10 and 6mm notch height (top to bottom).

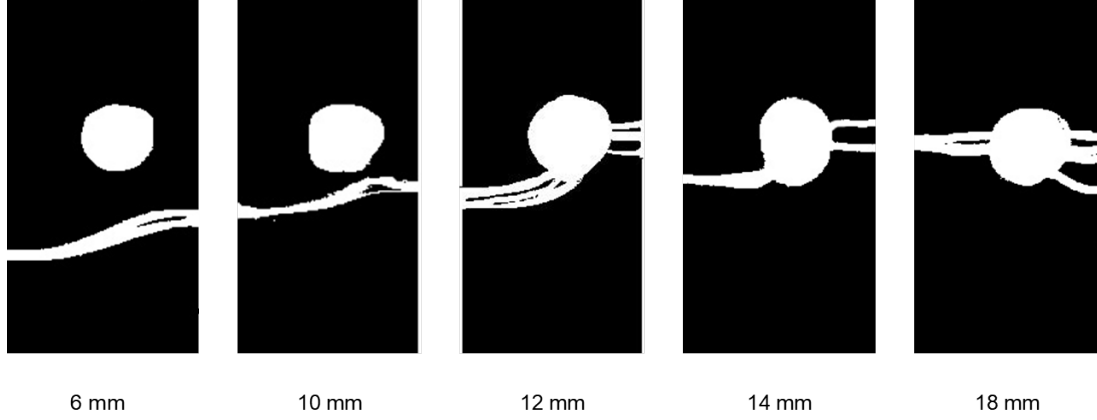


Figure 6: Evaluation of the averaged crack paths (4 to 6 experiments, cf. Figure 5) of the tested punctured EPDM strips with given notches at a height of 6, 10, 12, 14 and 18 mm measured from the bottom boundary above the bottom bulges (left to right).

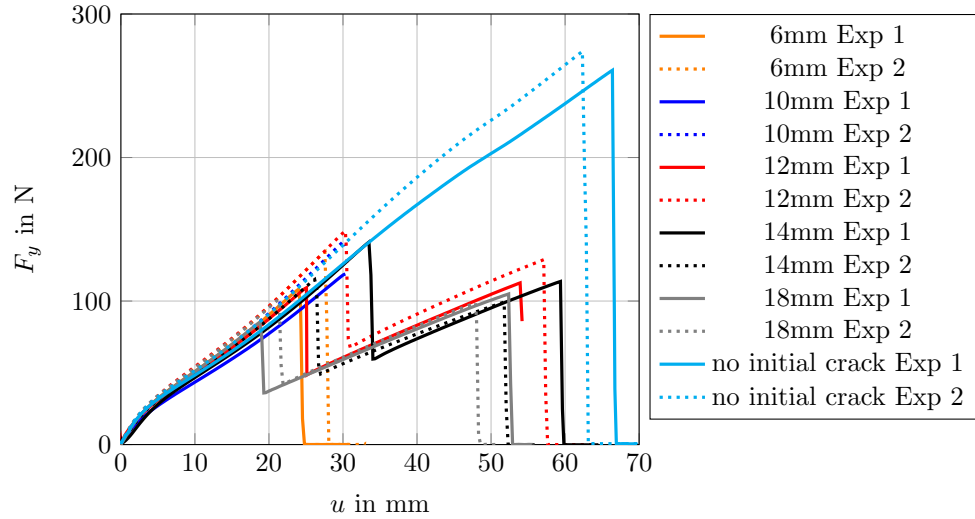


Figure 7: Two force-displacement curves for each notch height and test runs without an initial notch. Force response F_y in relation to the traverse displacement u measured in y -direction on the top boundary of the EPDM strips.

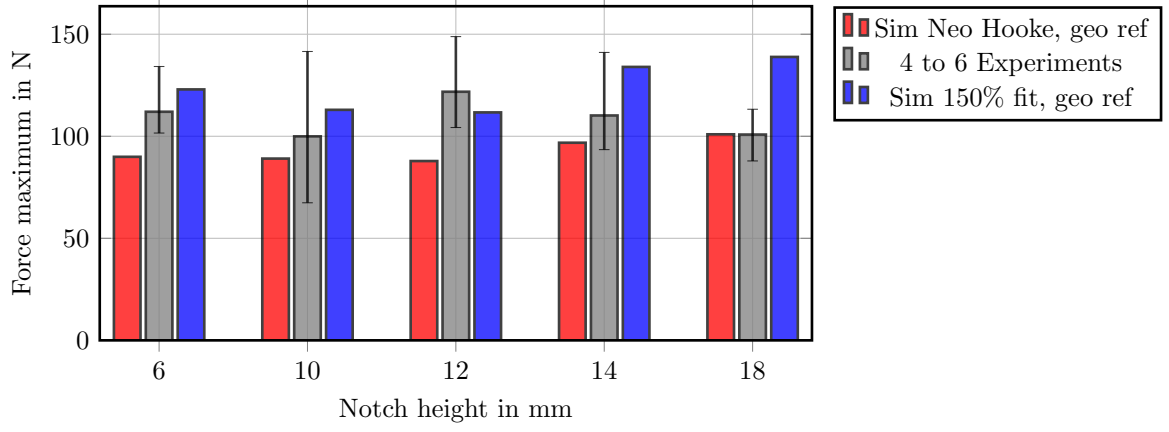


Figure 8: Maximal loading force F_y at the crack start measured on the top boundary, of experiments and finite element simulations. In gray (middle bar for each test), the averaged force maximum of 4 to 6 experiments in dependence of traverse displacement. In red and blue (left and right for each notch height), the numerically achieved force maxima are given.

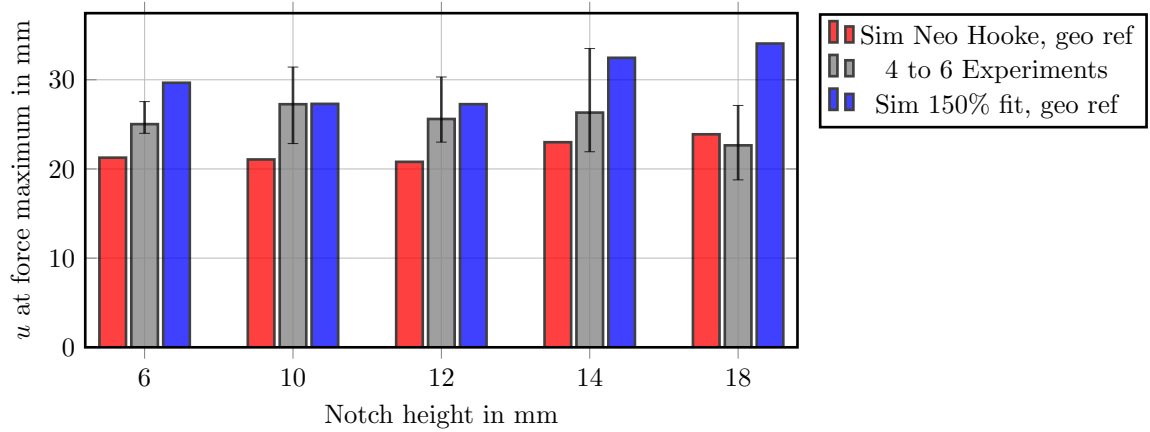


Figure 9: Traverse displacement u in y -direction at the first force maximum of experiments and finite element simulations. In gray (middle bar) the average displacement of (4 to 6) experiments, in red and blue (left and right bar for each notch height), the numerically achieved displacements at the first force maximum are given.

Later in 2014, Bourdin et al. [39] introduced a very similar functional with a stress-softening behavior and where the damage model remains purely elastic without damage until the stress reaches the critical value. This functional for complex cracks is defined as

$$AT_1 : \quad E_\epsilon(u, \varphi) = \int_{\Omega} \frac{g(\varphi)}{2} \sigma(u) : E_{lin}(u) dx + \int_{\Omega} \frac{3G_c}{8} \frac{1-\varphi}{\epsilon} dx + \int_{\Omega} \frac{3G_c}{8} \epsilon |\nabla \varphi|^2 dx. \quad (3)$$

Aside from different coefficients, Wu's energy functional in Equation (1) in comparison to the functionals in the Equations (2) and (3) uses a combination of a linear and a quadratic part in the second crack energy term, which yields the theoretically and numerically useful property of a finite support for a localized phase-field [16]. The numerical consequences of this choice are described in Section 4.3.

The Euler-Lagrange equations of Wu's energy functional in Equation (1) look like follows:

Problem 1 (Coupled variational inequality system of Wu's energy functional) Find $\varphi \in \mathcal{K}$ and $u \in \mathcal{V}$, such that

$$\begin{aligned} (g(\varphi)2\mu E(u), E(w)) + (g(\varphi)\lambda \text{tr} E_{lin}(u) \mathbf{I}, E_{lin}(w)) &= 0 \quad \forall w \in \mathcal{V}, \\ (1-\kappa)(\varphi 2\mu E_{lin}(u) : E_{lin}(u), \psi - \varphi) + (1-\kappa)(\varphi \lambda \nabla \cdot u \mathbf{I} : E_{lin}(u), \psi - \varphi) \\ &+ \frac{2G_c}{\pi} \left(-\frac{1}{\epsilon} \varphi, \psi - \varphi\right) + \frac{2G_c}{\pi} \epsilon (\nabla \varphi, \nabla(\psi - \varphi)) \geq 0 \quad \forall \psi \in \mathcal{K}. \end{aligned} \quad (4)$$

Based on the coupled variational inequality system (4), a mixed phase-field fracture model is developed in the following.

3.2 Mixed phase-field fracture model

For a mixed form of the problem, we define a hydro-static pressure $p \in \mathcal{U}$

$$p := \lambda \text{tr} (E_{lin}(u)),$$

such that the pure elasticity equation in weak form reads as:

Problem 2 (Pure elasticity) Assume $\varphi \in \mathcal{K}$ to be given. Find $u \in \mathcal{V}$ and $p \in \mathcal{U}$ such that

$$g(\varphi)2\mu (E_{lin}(u), E_{lin}(w)) + g(\varphi)(\nabla \cdot w, p) = 0 \quad \forall w \in \mathcal{V}, \quad (5)$$

$$g(\varphi)(\nabla \cdot u, q) - \frac{1}{\lambda}(p, q) = 0 \quad \forall q \in \mathcal{U}. \quad (6)$$

We refer the reader to [24] for details on the inf-sup stable mixed form of the elasticity equation.

Remark 2 (Degradation in the crack) To avoid non-physical pressure values in the inner fracture zone, the degradation term $g(\varphi)$ is neglected in the second term of Equation (6). It follows, if we are in the broken zone $\varphi = 0$, we are not fully divergence-free. This modification is an extension of our own recent model [24].

The variational formulation in Problem 1 and Problem 2 of the isotropic model given by Bourdin et al. [14] does not allow to distinguish between fracture behaviour in tension and compression [20]. In the following, we consider the volumetric and deviatoric contributions of the elastic energy density separated into σ^+ and σ^- to prevent interpenetration of the crack faces under compression [20], along to Amor et al. [19]. For this reason, the positive part of the pressure $p^+ \in L_2(\Omega)$ as well as the positive part of $E_{lin}^+(u)$ have to be defined as $p^+ := \max\{p, 0\}$ and $E_{lin}^+(u) := \max\{E_{lin}(u), 0\}$ as the maximum function, such that the stress tensor $\sigma(u, p)$ is split into:

$$\begin{aligned} \sigma^+(u, p) &:= \mu \max\{0, \text{tr}(E_{lin}^+(u))\} \mathbf{I} + 2\mu \left(E_{lin}^+(u) - \frac{1}{3} \text{tr}(E_{lin}^+(u)) \mathbf{I} \right) + p^+ \mathbf{I}, \\ \sigma^-(u, p) &:= \mu (\text{tr}(E_{lin}^+(u)) - \max\{0, \text{tr}(E_{lin}^+(u))\}) \mathbf{I} + (p - p^+) \mathbf{I}. \end{aligned}$$

Remark 3 The mixed quasi-static phase-field fracture model developed and used in previous contributions [24, 40, 41], is derived from the anisotropic phase-field fracture model with a spectral decomposition of the strain tensor along to Miehe et al. [42]. Based on this model promising numerical results considering benchmark tests in compressible and (nearly) incompressible solids could be presented. In the work on hand, the phase-field fracture model is applied to simulate a more complex crack propagation in nearly incompressible EPDM rubber, where the volumetric-deviatoric split of Amor et al. [19] allows more realistic numerical results. We refer the reader to Ambati et al. [20], who discuss the very similar numerical results for both energy splitting approaches. Nevertheless, the computational effort of the volumetric-deviatoric strain energy split is minor than for the spectral decomposition of the strain tensor.

From that, our newly introduced mixed phase-field fracture problem based on Wu's energy functional and strain energy splitting of Amor et al. in incremental form is formulated as:

Problem 3 (Mixed phase-field formulation) *Let the previous loading step data $\varphi^{n-1} \in \mathcal{K}$ be given. Find $u := u^n \in \{u_D + \mathcal{V}\}$, $p := p^n \in \mathcal{U}$ and $\varphi := \varphi^n \in \mathcal{K}$ for the loading steps $n = 1, 2, \dots, N$ such that*

$$g(\varphi^{n-1}) (\sigma^+(u, p), E_{lin}(w)) + (\sigma^-(u, p), E_{lin}(w)) = 0 \quad \forall w \in \mathcal{V}, \quad (7)$$

$$g(\varphi^{n-1}) (\nabla \cdot u, q) - \frac{1}{\lambda} (p, q) = 0 \quad \forall q \in \mathcal{U}, \quad (8)$$

$$(1 - \kappa) (\varphi \sigma^+(u, p) : E_{lin}(u), \psi - \varphi) + \frac{2G_c}{\pi} \left(-\frac{1}{\epsilon} \varphi, \psi - \varphi \right) + \frac{2G_c}{\pi} \epsilon (\nabla \varphi, \nabla (\psi - \varphi)) \geq 0 \quad \forall \psi \in \mathcal{K}. \quad (9)$$

Remark 4 *In the elasticity Equations (8) and (9), time-lagging is used in the phase-field variable φ to obtain a convex functional. Specifically, we notice that of course a time-discretization error of the order of the time step size (loading increment) arises. For fast growing cracks this makes a significant difference as shown in [43]. By applying subiterations, the discretization error can be reduced [23][Chapter 7.7].*

To the best of our knowledge, the phase-field fracture model derived from Wu's energy functional in Equation (1) with a mixed variational formulation of the elasticity equation, has not been considered in the literature so far. The numerical handling of the coupled phase-field fracture system with an inequality constraint in Problem 3 with the help of a monolithic solving approach including the discretization and two different refinement strategies are discussed in the following.

3.3 Numerical treatment, implementation, and programming code

The crack irreversibility, i.e., the variational inequality in the phase-field part is fulfilled with a primal-dual active set method; see [44] for further details. The overall nonlinear problem is solved with a Newton method and derived as a joint quasi-monolithic approach combined with the primal-dual active set method [44]. We notice that the nonlinear monolithic solution is challenging and different studies have appeared [43, 44, 45, 46, 47, 48, 49, 50, 51, 52].

For the spatial discretization, we employ a Galerkin finite element method in each incremental step, where the domain Ω is partitioned into quadrilaterals. To fulfill a discrete inf-sup condition, stable Taylor-Hood elements with bi-quadratic shape functions (Q_2) for the displacement field u and bilinear shape functions (Q_1) for the pressure variable p and the phase-field variable φ are used as in [24].

The implementation of the proposed problem formulation is derived from the open-source code <https://github.com/tjhei/cracks>. Further details on the code are given in [53, 54]. This 'pfm-cracks' project is based on deal.II [55] and provides to simulate crack propagation in elastic and porous media. Starting from the classical phase-field fracture model with two unknowns, the displacements and the phase-field variable discretized with $Q_1 Q_1$ elements, we implemented the mixed problem formulation with Taylor-Hood elements $Q_2 Q_1$ elements for the elasticity pair (u, p) . We end up with three unknowns u, p and φ discretized with $Q_2 Q_1 Q_1$ finite elements and solve the variational inequality system by help of a primal-dual active set scheme. Further, we set up the new test considering the punctured EPDM strips till total failure with proper boundary and initial conditions, and implemented the required functionals of interest to allow comparing numerical and experimental results.

For a spatial convergence study in Section 4.1, a predictor-corrector scheme is used along to [44, Chapter 4] for adaptive mesh refinement. This refinement scheme allows to refine the mesh locally depending on a propagating fracture with a chosen threshold (here $\rho = 0.7$) for the phase-field variable: when the crack phase-field on a coarse cell has values smaller than 0.7, the mesh on this cell is refined and the incremental step is computed again on an adaptive mesh, where the cell with $\varphi < 0.7$ is refined in dependence of its neighbour cells. This allows to give a sharp crack while having a reasonable amount of workload, because the mesh is just refined, if we have a change in the phase-field variable which pictures the crack area. In further numerical tests in Section 4.2, geometrically preredefined meshes are used to avoid observed mesh locking around the circular hole and to guarantee a good resolution also towards the top boundary where we evaluate the loading force as one quantity of interest.

4 Numerical simulation of crack propagation in punctured EPDM strips

Crack propagation in Section 2 is observed via stretching the punctured EPDM strips until total failure with a speed of 200mm/min. For the numerical simulation of the crack propagation in punctured strips in a two-dimensional setup (plane stress assumption) with help of the phase-field fracture model from Section 3.2, we reduce the geometry to the area of interest between the bulges on the bottom and top part where the specimens are fixed. The geometry is given in Figure 10. Considering holes in a material combined with phase-field fracture modeling is still a challenging task and not fully understood; see [21, Section 8.2] for further comments on the difficulty of inclusions. Homogeneous Dirichlet boundary conditions $u_y = 0$ are chosen on the top boundary and the strips are fixed in horizontal direction on the top and bottom boundary via $u_x = 0$. The following boundary condition characterizes the loading force on the bottom boundary Γ_{force} in y -direction:

$$u_y = t \cdot 200\text{mm/min}, \text{ for } t \in \mathcal{I} := [0; \text{total failure}], \quad (10)$$

where t denotes the total time. In the quasi-static context, the time interval \mathcal{I} is divided into incremental steps of size δt . Further, the phase-field is fixed via $\varphi = 0$ in the given notch as an initial boundary condition.

Remark 5 (Numerical handling of given notch) *We decided to handle the given notch on the left side of size 1mm with an initial condition $\varphi = 0$ such that the material is already broken in the notch area. In addition, we describe the initial crack by doubling the degrees of freedom on the respective faces similar to Wick [46, Section 5.1.]. This allows the material to open in the notch and the maximal stress is obtained in the notch tip, which in turn imitates the observed opening of the notch in the running experiments.*

The numerical parameters are listed in Table 3.

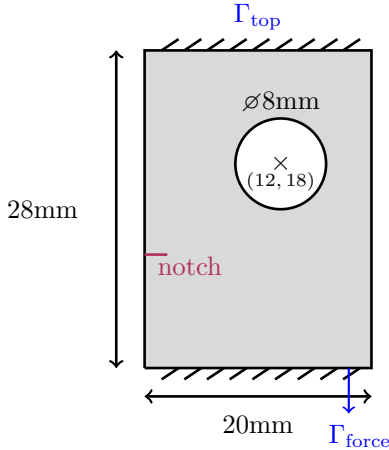


Figure 10: Geometry and boundary conditions of punctured EPDM strips. Loading force on Γ_{force} defined in Equation (10).

Parameter	Description	Value
h	discretization parameter (coarsest)	0.3mm
$\# \text{ ref}$	number of adaptive refinement steps	0 to 3
ρ	phase-field threshold for refinement	0.7
ϵ	bandwidth	$2h$
δt	incremental size	10^{-2}s
κ	regularization parameter	$0.01h$

Table 3: Numerical parameters for the phase-field fracture simulation of punctured EPDM strips. Parameters ' $\# \text{ ref}$ ' and ' ρ ' required for the adaptive test runs in Section 4.1. The numerical parameters $h, \epsilon, \delta t$ and κ are valid for all numerical test runs.

The setting of the numerical parameters in Table 3 is valid for all numerical results considering the spatial convergence study with the 6mm test using adaptive refinement. The incremental size δt and the size of κ is the same for all numerical tests. Related to the material parameter setting, we choose two cases of Figure 1 and Table 2. The coloured material parameters in Table 2 reflect the parameter settings based on two different assumptions for a linear E : the Young's modulus estimated via a Neo Hookean model and a fit of 150% of the strain. In all following numerical results and especially in the figures of this section the setting of the material parameters is differed via naming it '150% fit' or 'Neo Hooke', respectively. The bulk modulus $K = 2595\text{MPa}$ listed in Table 2 is specified via an averaged value of the fitted values in Figure 2. The critical energy release rate is adopted from Figure 4 such that $G_c = 17.0\text{N/mm}$.

Quantities of interest. To compare the experimental and numerical results, we consider two quantities of interest: first, the solution of the phase-field after total failure and the crack paths in the punctured strips. As a second quantity,

we compare for proper test cases the force-displacement curves of the experiments and simulations to retrace the crack propagation process.

Relative to the force-displacement curves, the load vector on the top boundary Γ_{top} is evaluated via

$$(F_x, F_y) := \frac{1}{|\Gamma_{\text{top}}|} \int_{\Gamma_{\text{top}}} \sigma(u)n \, ds, \quad (11)$$

with the length $|\Gamma_{\text{top}}| = 20\text{mm}$ of the top boundary, the stress tensor $\sigma(u) := 2\mu E_{\text{lin}}(u) + \lambda \text{tr}(E_{\text{lin}}(u))\mathbf{I}$ and the normal vector n . Within the EPDM tests we are interested in the loading force F_y on Γ_{top} , where the force response is also measured in the experiments.

4.1 Spatial convergence study

To study spatial convergence of the finite element simulation, we start with a series of tests for one of the five test setups: the given notch is at a height of 6mm, where experimentally we do not expect the crack propagating towards the hole but in a 'S'-curve from the left to the right. For this example, four test runs are conducted, first on a global prrefined mesh with a discretization parameter $h_{\text{start}} = 0.3\text{mm}$ and three tests with 1 to 3 adaptive refinement steps. The numerical results are given in Figure 4.1. The number of degrees of freedom (DoF) for all conducted tests runs of spatial convergence are listed in Table 4. While refining the area around the crack adaptively along to the predictor-corrector scheme from [44], or in other words, while decreasing h locally, the length scale parameter ϵ is fixed. To get an idea how the predictor-corrector scheme works within the propagating fracture, for one test of the series (6mm, Neo Hooke, hole), the meshes at five certain loading points are given in Figure 12. Consequently, for all computations considered in Figure 11, it holds $\epsilon = 0.6\text{mm}$. Further, the results for both parameter settings '150% fit' and 'Neo Hooke' are given.

Beside of spatial convergence, we want to avoid locking effects that could arise around the circular hole. The test with a notch at 6mm height gives a crack path away from the hole, even if the inclusion has an impact on the crack pattern. The refinement series is also conducted for both different material parameter settings (Neo Hooke and 150% strain fit) without the inclusion.

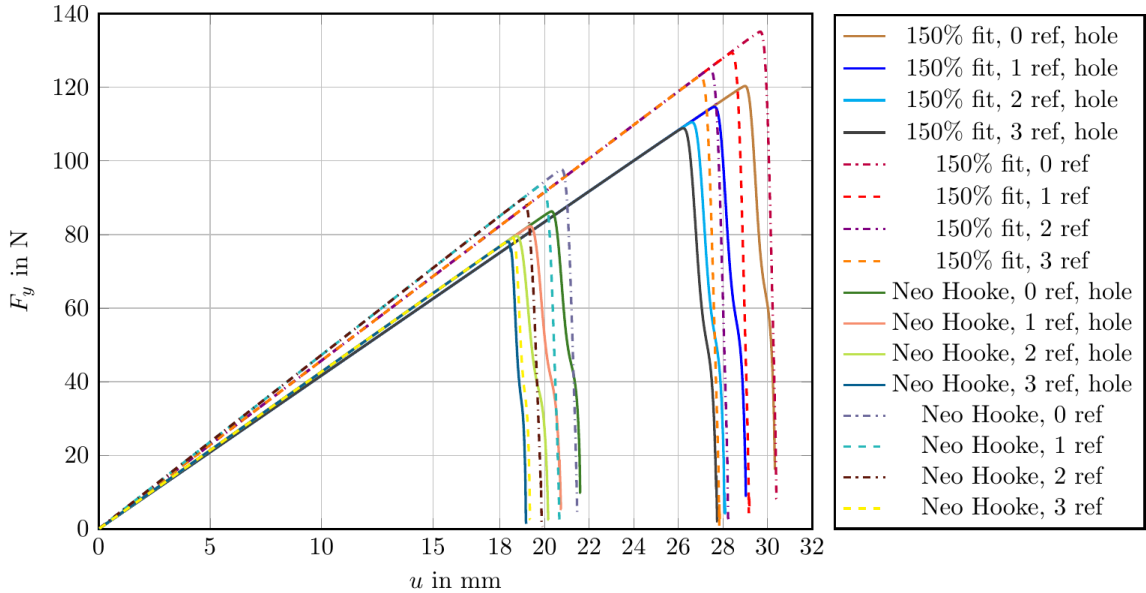


Figure 11: Numerical refinement study: force-displacement curves (displacement u in y -direction versus force F_y) for the EPDM benchmark test based on the material parameters of Table 2 (150% fit of strain) compared the material parameters of Table 2 with a notch at 6mm, $h_{\text{start}} = 0.3$ and $\epsilon = 2h_{\text{start}} = 0.6\text{mm}$ fixed. $G_c = 17.0\text{N/mm}$. The computation of the force response F_y on the top boundary is defined in Equation (11).

In total, three points are observed in Figure 11:

- We compare the results based on the Neo Hookean material parameters from Table 2 with the computation based on the 150% strain fit assumption.
- The results are given based on the geometry in Figure 10 with a given notch and a circular hole in the upper right part of the strips compared to results based on the same geometry with a given notch but without a hole. The results in Figure 11 for the punctured strips are marked with the attribute 'hole' in the legend.
- The third point discussed in Figure 11, is spatial convergence of the force-displacement curves with an increasing number of adaptive refinement steps, while the crack width ϵ is fixed as in Table 3 even if h is getting smaller in the crack area. In the legend in Figure 11 the number of refinement steps ('# ref') is given for each force-displacement curve.

It can be observed that the gradient towards the force maximum in the results based on the punctured strips is steeper than without a circular inclusion. From this, one could follow, that the inclusion makes the material more elastic and decreases the material stiffness. Further, a significant difference between the force-displacement curves of the tests based on the 150% fit or Neo Hookean material parameters can be observed. All Neo Hookean tests have a lower maximal force, which leads to a smaller displacement when the crack starts propagating, cf. Figures 8 and 9. Further in Figure 11 one can observe spatial convergence within a series of tests from 0 to 3 adaptive refinement steps.

Test (name)	#DoF u	(#DoF p) = (#DoF φ)
6mm, 150% fit & Neo Hooke, 0 ref, hole	49,984	6,352
6mm, 150% fit, 1 ref, hole	65,284	8,277
6mm, 150% fit, 2 ref, hole	117,400	1,4815
6mm, 150% fit, 3 ref, hole	304,786	38,288
6mm, 150% fit, 0 ref	51,906	6,577
6mm, 150% fit, 1 ref	70,376	8,898
6mm, 150% fit, 2 ref	135,220	17,028
6mm, 150% fit, 3 ref	369,498	46,359
6mm, Neo Hooke, 1 ref, hole	65,420	8,294
6mm, Neo Hooke, 2 ref, hole	119,396	15,067
6mm, Neo Hooke, 3 ref, hole (Fig. 12)	293,572	36,880
6mm, Neo Hooke, 0 ref	51906	6,577
6mm, Neo Hooke, 1 ref	70,446	8,907
6mm, Neo Hooke, 2 ref	136,742	17,308
6mm, Neo Hooke, 3 ref	371,840	46,650
Figure 14	237,436	29,877
Figure 15	391,656	49,192
Figure 16	427,932	53,731
Figure 17	437,544	54,934
Figure 18	581,724	72,979

Table 4: Number of degrees of freedom (DoF) for all numerical test runs in Figure 11, and the Figures 14 to 18 for the displacement u (Q_2 -elements) and the pressure variable p (Q_1 -elements), which has the same number of DoF as the phase-field variable φ (Q_1 -elements). The number of degrees of freedom for the test with adaptive predictor corrector mesh refinement from Figure 11 are given for the mesh at total failure in the last computed incremental step.

In Figure 13, the numerical force-displacement curves have a similar course as the experimentally achieved force-displacement curves. Here, not just the most converging results 'Neo Hooke, 3 ref' and '150% fit, 3 ref' from Figure 11 are given in Figure 13, but also the results from a second test run, where we geometrically preredefined two times the area from 2mm below the notch until 1mm above the circular hole in addition to a globally preredefined mesh with cell diameter $h = 0.3$. See Figure 18 for the finite element mesh used for the dashed and coloured force-displacement curves given in Figure 13. The force-displacement curves from the simulations computed on the geometrically preredefined meshes seem to give better results compared to the experiments than the results based on adaptively refined meshes and a fixed bandwidth ϵ . This observed mesh-sensitivity of phase-field fracture models is widely discussed in the literature, see for example in [20, 24, 44, 56, 46]. Further, one can see that the length scale ϵ , the ϵ - h relation as well as the incremental step size δt can have an impact on the accurate shape of the force-displacement curves also for very simple benchmark

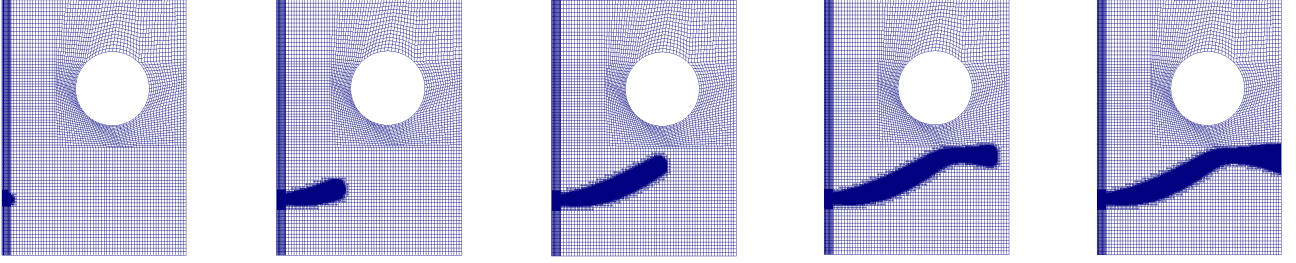


Figure 12: Adaptively refined meshes at five certain time points for the numerical simulation based on the Neo Hookean material parameter setting from Table 2 and three steps of adaptive refinement steps via the predictor-corrector scheme from [44], cf. the blue-green curve in Figure 11. In the last snapshot, the mesh contains 79,954 DoF for the solid displacements and 10,160 DoF for the pressure and the phase-field variable.

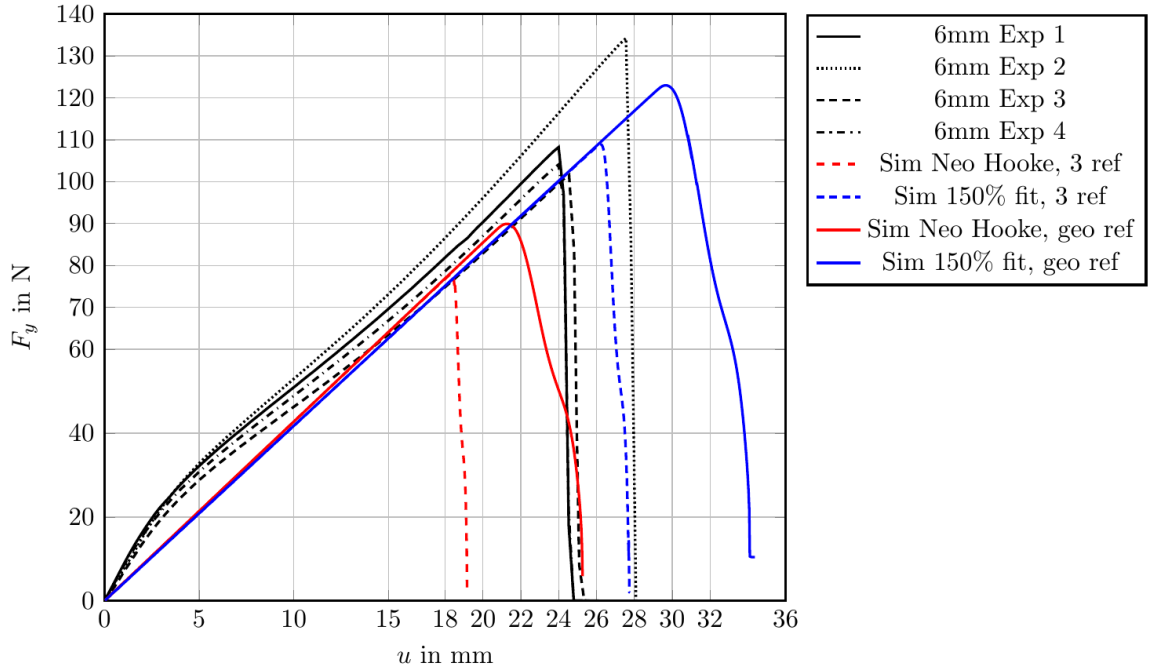


Figure 13: Comparison of the force-displacement curves (displacement u in y -direction versus force F_y) for the samples with a notch at 6mm height (experiments 'Exp 1' to 'Exp 4' versus simulations).

tests. Further analysis on this topic is beyond the scope of this work and will be addressed in future.

4.2 Crack paths comparison

In Figure 14 to 18, the phase-field functions for five different notch heights are given in comparison to the experimental crack paths after total failure. The finite element meshes are geometrically preredefined generously including the hole and the given notch. The used numbers of degrees of freedom in Figure 14 to 18 are listed in the lower part of Table 4. For the tests with a given notch at 18mm, 14mm, 12mm and 6mm, the crack paths of the simulation coincide sufficiently with the average crack paths from 4 to 6 conducted experiments in the Figures 14, 15, 16 and 18. Furthermore, the numerically achieved crack paths for the two different parameter settings 'Neo Hooke' and '150% fit' are very similar for all five tests with different notch heights. Just the location and the angle from where the crack passes the circular inclusion varies slightly, see for example Figure 16. In Figure 17, snapshots of the phase-field function for both parameter settings are given for the test with a notch at 10mm. Observing the experiments for this test case, the crack propagates close to hole but not into the hole. Compare also Figure 5 for the 10mm test (second row from the bottom), especially the first, third and fourth test specimen, where the crack propagates very close to the hole. The phase-field fracture simulation shows a fracture path similar to them of the 14 and 18mm tests. One reason could be, that the crack width ϵ is, from a numerical point of view, not small enough to allow cracks very close to the boundary of the hole without cracking into it.

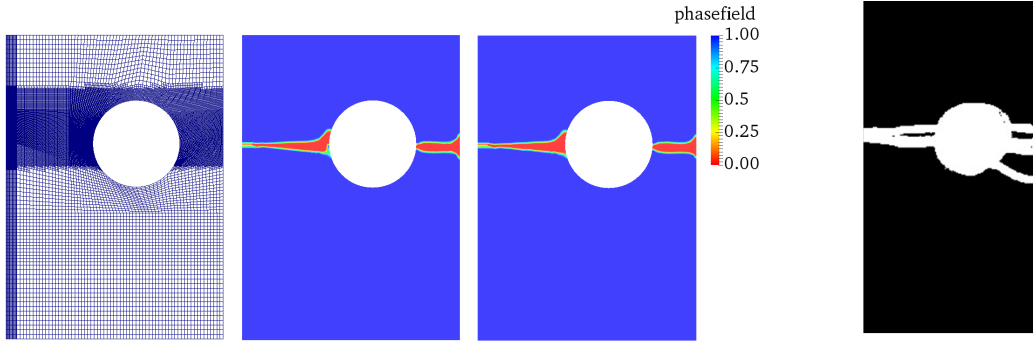


Figure 14: Snapshots of the phase-field function after total failure compared to the experimental results for the samples with a notch at 18mm height. From left to right: the geometrically preredefined mesh, the phase-field function based on the Neo Hookean parameter setting from Table 2, the phase-field function based on the 150% strain fit parameter setting from Table 2, the experimental results from 5 executed experiments.

In the numerical results in Figure 14 to 17, we observe that the location, where the crack propagates from the hole to the right boundary of the EPDM strips, is in the very middle of the hole and goes straight to the right (shortest way for the crack) while in the experiments the angles and paths of the crack paths on the right of the hole vary a lot, cf. Figures 14.

4.3 Comment on our choice of energy functional and strain energy splitting

Our choice of the energy functional design as well the strain energy splitting in Section 3 is deliberately fitted to the experiments in Section 2. We made the experience that even with a given notch, the crack starts propagating from the circular hole in the inner of the EPDM strips and propagates simultaneously to the left and right, if the mixed phase-field fracture model is based on an Ambrosio-Tortorelli functional [15, 36] (AT₁ or AT₂, see [38] for a comparison of AT₁ and AT₂ considering crack nucleation) and the elastic energy splitting approach of Miehe [57]. This high sensitivity around the inclusion also for a very small incremental size δt and proper adaptive refinement schemes led us to the energy functional of Wu [16] and Amor's volumetric-deviatoric energy splitting [19]. In the literature, for example in [21], a pre-cracked sample with two holes is presented in a compressible solid. Beside the fact, that depending on the mesh, the boundary conditions, initial conditions and the underlying phase-field model, very different crack path results are presented. Further, they point out the need of further studies on problems with holes and inclusions in in [21, Section 8.2]. Other references on computing and discussing crack propagation in solids with inclusions are [58, 59, 27, 60]. The last two cited groups are also considering (nearly) incompressible materials.

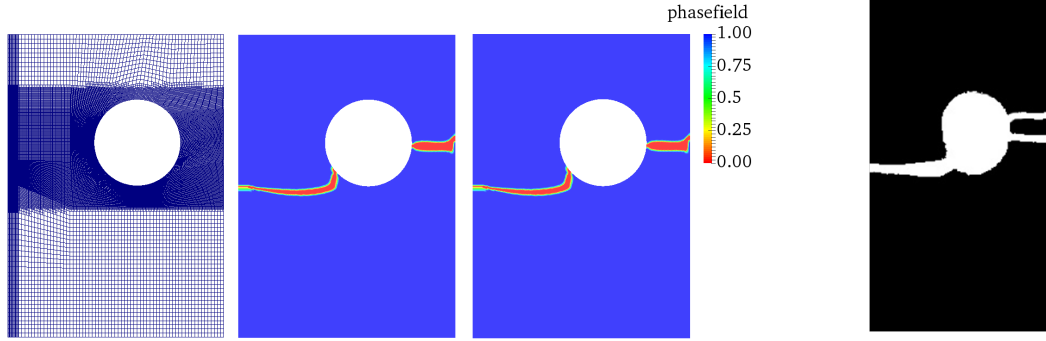


Figure 15: Snapshots of the phase-field function after total failure compared to the experimental results for the samples with a notch at 14mm height. From left to right: the geometrically prerefined mesh, the phase-field function based on the Neo Hookean parameter setting from Table 2, the phase-field function based on the 150% strain fit parameter setting from Table 2, the experimental results from 4 executed experiments.

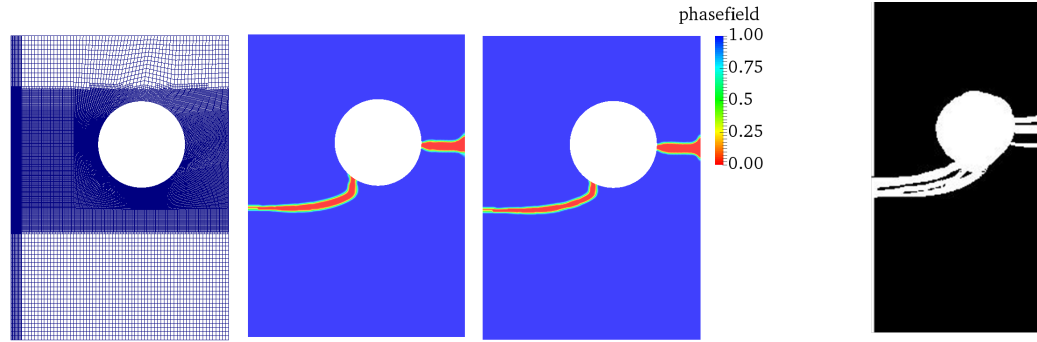


Figure 16: Snapshots of the phase-field function after total failure compared to the experimental results for the samples with a notch at 12mm height. From left to right: the geometrically prerefined mesh, the phase-field function based on the Neo Hookean parameter setting from Table 2, the phase-field function based on the 150% strain fit parameter setting from Table 2, the experimental results from 4 executed experiments.

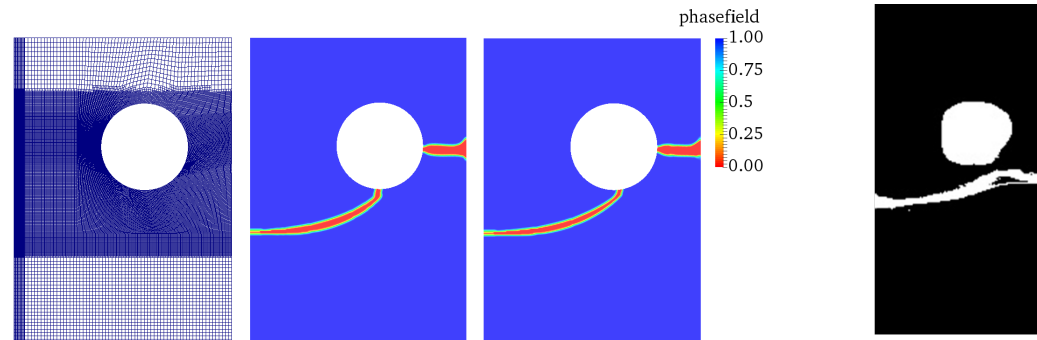


Figure 17: Snapshots of the phase-field function after total failure compared to the experimental results for the samples with a notch at 10mm height. From left to right: the geometrically prerefined mesh, the phase-field function based on the Neo Hookean parameter setting from Table 2, the phase-field function based on the 150% strain fit parameter setting from Table 2, the experimental results from 6 executed experiments.

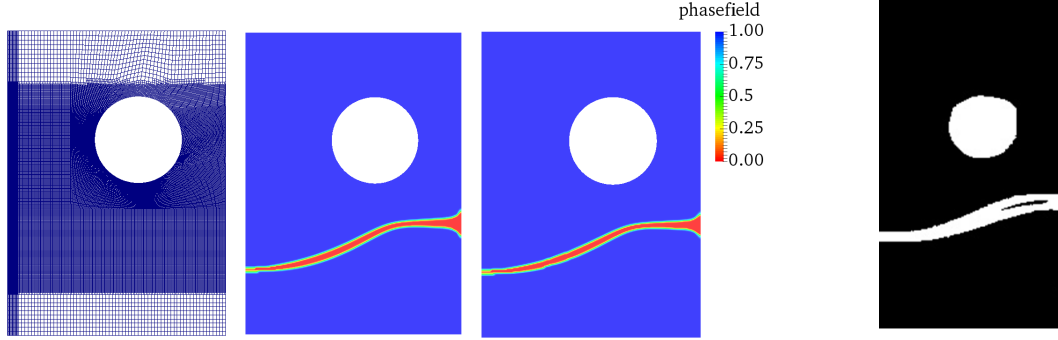


Figure 18: Snapshots of the phase-field function after total failure compared to the experimental results for the samples with a notch at 6mm height. From left to right: the geometrically preredefined mesh, the phase-field function based on the Neo Hookean parameter setting from Table 2, the phase-field based on the 150% strain fit parameter setting from Table 2, the experimental results from 4 executed experiments.

5 Discussion of experimental and numerical results

Despite the assumed simplifications related to geometrical and material non-linearities, the model is able to capture the behavior at least qualitatively. The experimental data related to the tracking of the crack paths as well as the respective numerical simulations suggest a clear dependency on the position of the initial crack position, which can be confirmed by the numerical simulations. In the bottom row in Figure 5 as well as in Figure 18 one can see that even for an initial crack near the lower boundary (6mm) far from the hole, the influence of the inhomogeneous stress/strain field is still apparent. The crack starts perpendicularly to the direction of tension on the right side (here: back side), but is diverted upwards later on and returns to a perpendicular path in the end.

This effect is observed in the experimental data till initial cracks with a notch height of 10mm. At the end of the crack path for specimens marked with #7 (second row from below), the path is diverted downwards. In the finite element simulation, the crack path within the 10mm test differs such that the crack propagates into the hole as also seen in the 12, 14 and 18mm tests. For initial cracks at 12 and 14mm height, the path proceeds in a curved shape into the hole and continues perpendicular on the other side of it. At 18mm height, approximately on position of the circle's center, the initial crack propagates directly perpendicular into the hole and propagates likewise on the other side until complete rupture. The same can be observed in the numerical results for the tests with a notch height of 12, 14 and 18mm. Evaluating the statistics of the experiments, repeatability is given. The repetitions of the tests indicate that minor variations, e.g. small changes in the initial crack length or its angle will have small effects on the general crack path as well. Although dealing with a carbon black filled rubber, no bifurcations in the crack paths for the EPDM compound were observed. Due to the high variation in the onset of total failure in the experiments the calibration of related phase-field parameters might be tricky in the future.

6 Conclusions

In this work, a phase-field fracture model in mixed form is proposed to simulate crack propagation in EPDM rubber considering the crack path behavior. The model is based on a mixed form of the solid equation derived from Wu's energy functional [16] and the anisotropic model of Amor et al. [19] with a volumetric-deviatoric strain energy splitting, matching the volume conservation of incompressible materials. The obtained crack paths in the numerical results compared to the punctured EPDM strips after stretching them with a certain load until total failure, coincide aside from experimental scattering and the inaccuracy in phase-field fracture modeling with respect to the smeared transition zone around the crack. Even if a quasi-static phase-field fracture model assuming linear elasticity is used for simulating crack propagation in punctured EPDM strips with a given notch, the crack paths and force-displacement results are promising. Especially the crack paths coincide satisfactorily for the tests with a notch height of 18, 14, 12 and 6mm, see Figures 14, 15, 16 and 18, respectively. Furthermore, the force-displacement curves, as an example for the 6mm test, are similar to the experimentally achieved curves, especially with respect to the maximum force at the crack start (Figure 8) and the traverse displacement at the maximum force (Figure 9) within the natural scattering of the experiments. However, we stress that most of our comparisons are of qualitative nature because of simplifications in the governing material models such as nonlinear behavior. Due to the complexity of the experimental and numerical setups, our results are nonetheless a major advancement and themselves novel in the published literature.

In future work, a dynamic phase-field fracture model will be considered. Further, a detailed analysis on the mesh sensitivity and ϵ - h relation in simulating crack propagation in rubber-like materials will be addressed. In addition, considering the high non-linear behavior of filled rubbers in cyclic applications, non-linear geometrical effects as well as non-linear material effects have to be addressed. Further, in cyclic dynamic loadings viscoelasticity, temperature effects due to energy dissipation, static hysteresis and permanent deformations become more relevant. Several models to describe those effects are benchmarked in [61], see also [62]. Perspectively, the combination of sophisticated mechanical material models and phase field fracture models for describing the crack propagation in rubbers seems promising.

Acknowledgments

The authors would like to thank P  n  lope Barb  ry (student at ENSTA Bretagne, Brest) for her support in conducting some of the experiments during her internship at DIK. Further, the work has been supported by the German Research Foundation, Priority Program 1748 (ID 392587580, WI 4367/2-1).

References

- [1] A. W  hler,   ber die Festigkeitsversuche mit Eisen und Stahl, *Zeitschrift f  r Bauwesen* 20 (1870) 73–106.
- [2] O. Gehrmann, N. H. Kr  ger, M. Krause, D. Juhre, Dissipated energy density as fatigue criterion for non-relaxing tensional loadings of non-crystallizing elastomers?, *Polymer Testing* 78 (2019) 105953 (online).
- [3] M. Ludwig, Entwicklung eines Lebensdauer-Vorhersagekonzepts f  r Elastomerwerkstoffe unter Ber  cksichtigung der Fehlstellenstatistik, Dissertation, Universit  t Hannover (2017).
- [4] M. El Yaagoubi, D. Juhre, J. Meier, N. H. Kr  ger, T. Alshuth, U. Giese, Lifetime prediction of filled elastomers based on particle distribution and the j-integral evaluation, *International Journal of Fatigue* 112 (2018) 341–354.
- [5] O. Gehrmann, M. El Yaagoubi, H. El Maanaoui, J. Meier, Lifetime prediction of simple shear loaded filled elastomers based on the probability distribution of particles, *Polymer Testing* 75 (2019) 229–236.
- [6] J. Lemaitre, A continuous damage mechanics model for ductile fracture, *Journal of Engineering Materials and Technology* 107 (1) (1985) 83–89.
- [7] J. Grandcoin, A. Boukamel, S. Lejeunes, A micro-mechanically based continuum damage model for fatigue life prediction of filled rubbers, *International Journal of Solids and Structures* 51 (6) (2014) 1274–1286.
- [8] P. Charrier, E. Ostoj  -Kuczyński, E. Verron, G. Marckmann, L. Gornet, G. Chagnon, Theoretical and numerical limitations for the simulation of crack propagation in natural rubber components, *Constitutive Models for Rubber III* (2003) 3–10.
- [9] C. Timbrell, M. Wiehahn, G. Cook, A. H. Muhr, Simulation of crack propagation in rubber, *Constitutive Models for Rubber III* (2003) 11–20.
- [10] M. Kaliske, R. Behnke, R. Fleischhauer, K.   zenc, I. M. Zreid, Thoretical-numerical approaches to simulate fracture in polymeric materials, *Procedia Materials Science* 3 (2014) 2065–2070.
- [11] A. Griffith, The phenomena of flow and rupture in solids, *Transactions of the Royal Society A* 221 (1920) 163–198.
- [12] G. Francfort, J.-J. Marigo, Revisiting brittle fracture as an energy minimization problem, *Journal of the Mechanics and Physics of Solids* 46 (8) (1998) 1319–1342.
- [13] B. Bourdin, G. A. Francfort, J.-J. Marigo, The variational approach to fracture, *Journal of elasticity* 91 (1-3) (2008) 5–148.
- [14] B. Bourdin, G. A. Francfort, J.-J. Marigo, Numerical experiments in revisited brittle fracture, *Journal of the Mechanics and Physics of Solids* 48 (4) (2000) 797–826.
- [15] L. Ambrosio, V. M. Tortorelli, Approximation of functional depending on jumps by elliptic functional via t-convergence, *Communications on Pure and Applied Mathematics* 43 (8) (1990) 999–1036.
- [16] J.-Y. Wu, A unified phase-field theory for the mechanics of damage and quasi-brittle failure, *Journal of the Mechanics and Physics of Solids* 103 (2017) 72–99.
- [17] J.-Y. Wu, A geometrically regularized gradient-damage model with energetic equivalence, *Computer Methods in Applied Mechanics and Engineering* 328 (2018) 612–637.
- [18] J.-Y. Wu, V. P. Nguyen, A length scale insensitive phase-field damage model for brittle fracture, *Journal of the Mechanics and Physics of Solids* 119 (2018) 20–42.

- [19] H. Amor, J.-J. Marigo, C. Maurini, Regularized formulation of the variational brittle fracture with unilateral contact: Numerical experiments, *Journal of the Mechanics and Physics of Solids* 57 (8) (2009) 1209–1229.
- [20] M. Ambati, T. Gerasimov, L. De Lorenzis, A review on phase-field models of brittle fracture and a new fast hybrid formulation, *Computational Mechanics* 55 (2) (2015) 383–405.
- [21] J.-Y. Wu, V. P. Nguyen, C. T. Nguyen, D. Sutula, S. Bordas, S. Sinaie, Phase field modeling of fracture, *Advances in applied mechanics: multi-scale theory and computation* 52.
- [22] B. Bourdin, G. A. Francfort, Past and present of variational fracture, *SIAM News* 52 (9).
- [23] T. Wick, *Multiphysics Phase-Field Fracture: Modeling, Adaptive Discretizations, and Solvers*, Vol. 28, Walter de Gruyter GmbH & Co KG, 2020.
- [24] K. Mang, T. Wick, W. Wollner, A phase-field model for fractures in nearly incompressible solids, *Computational Mechanics* 65 (1) (2020) 61–78.
- [25] A. Fehse, N. H. Kröger, K. Mang, T. Wick, Crack path comparisons of a mixed phase-field fracture model and experiments in punctured epdm strips, *PAMM* 20 (1) (2020) pamm.202000335.
- [26] P. J. Loew, B. Peters, L. A. A. Beex, Fatigue phase-field damage modeling of rubber, *Constitutive Models for Rubber XI* (2019) 408–412.
- [27] P. J. Loew, B. Peters, L. A. A. Beex, Rate-dependent phase-field damage modeling of rubber and its experimental parameter identification, *Journal of the Mechanics and Physics of Solids* 127 (2019) 266–294.
- [28] A. Faye, Y. Lev, K. Y. Volokh, Modeling dynamic fracture in rubberlike materials, *Constitutive Models for Rubber XI* (2019) 505–511.
- [29] K. Y. Volokh, Fracture as a material sink, *Materials Theory* 1 (3) (2017) 1–9.
- [30] O. Gehrman, N. H. Kröger, P. Erren, D. Juhre, Estimation of the compression modulus of a technical rubber via cyclic volumetric compression tests, *Technische Mechanik* 37 (1) (2017) 28–36.
- [31] A. Ricker, N. H. Kröger, Influence of various curing systems and carbon black content on the bulk modulus of EPDM rubber, *Constitutive Models for Rubber XI* (2019) 200–205.
- [32] D. Roucou, J. Diani, M. Brieu, J. Witz, A. Mbiaskop-Ngassa, Experimental investigation of elastomer mode I fracture: An attempt to estimate the critical strain energy release rate using sent tests, *International Journal of Fracture* 209 (2018) 163–170.
- [33] D. Roucou, J. Diani, M. Brieu, A. Mbiaskop-Ngassa, Critical strain energy release rate for rubbers: single edge notch tension versus pure shear tests, *International Journal of Fracture* 216 (2019) 31–39.
- [34] D. Roucou, J. Diani, M. Brieu, A. Mbiakop-Ngassa, Impact of strain-induced softening on the fracture of a carbon-black filled styrene butadiene rubber, *Constitutive Models for Rubber XI* (2019) 528–532.
- [35] R. R. M. Ozelo, P. Sollero, A. L. A. Costa, An alternative technique to evaluate crack propagation path in hyperelastic materials, *Tire Science and Technology TSTCA* 40 (1) (2012) 42–58.
- [36] L. Ambrosio, V. Tortorelli, On the approximation of free discontinuity problems, *Bollettino dell’Unione Matematica Italiana* 6 (1) (1992) 105–123.
- [37] D. B. Mumford, J. Shah, Optimal approximations by piecewise smooth functions and associated variational problems, *Communications on pure and applied mathematics*.
- [38] E. Tanné, T. Li, B. Bourdin, J.-J. Marigo, C. Maurini, Crack nucleation in variational phase-field models of brittle fracture, *Journal of the Mechanics and Physics of Solids* 110 (2018) 80–99.
- [39] B. Bourdin, J.-J. Marigo, C. Maurini, P. Sicsic, Morphogenesis and propagation of complex cracks induced by thermal shocks, *Physical review letters* 112 (1) (2014) 014301.
- [40] S. Basava, K. Mang, M. Walloth, T. Wick, W. Wollner, Adaptive and pressure-robust discretization of incompressible pressure-driven phase-field fracture, *arXiv preprint arXiv:2006.16566*.
- [41] K. Mang, M. Walloth, T. Wick, W. Wollner, Adaptive numerical simulation of a phase-field fracture model in mixed form tested on an l-shaped specimen with high poisson ratios, *arXiv preprint arXiv:2003.09459*.
- [42] C. Miehe, F. Welschinger, M. Hofacker, Thermodynamically consistent phase-field models of fracture: variational principles and multi-field fe implementations, *International Journal for Numerical Methods in Fluids* 83 (2010) 1273–1311.
- [43] T. Wick, An error-oriented newton/inexact augmented lagrangian approach for fully monolithic phase-field fracture propagation, *SIAM Journal on Scientific Computing* 39 (4) (2017) B589–B617.

- [44] T. Heister, M. F. Wheeler, T. Wick, A primal-dual active set method and predictor-corrector mesh adaptivity for computing fracture propagation using a phase-field approach, *Computer Methods in Applied Mechanics and Engineering* 290 (2015) 466–495.
- [45] T. Gerasimov, L. D. Lorenzis, A line search assisted monolithic approach for phase-field computing of brittle fracture, *Computer Methods in Applied Mechanics and Engineering* 312 (2016) 276 – 303.
- [46] T. Wick, Modified newton methods for solving fully monolithic phase-field quasi-static brittle fracture propagation, *Computer Methods in Applied Mechanics and Engineering* 325 (2017) 577–611.
- [47] A. Kopanicakova, R. Krause, A recursive multilevel trust region method with application to fully monolithic phase-field models of brittle fracture, *Computer Methods in Applied Mechanics and Engineering* 360 (2020) 112720.
- [48] P. K. Kristensen, E. Martinez-Paneda, Phase field fracture modelling using quasi-newton methods and a new adaptive step scheme, *Theoretical and Applied Fracture Mechanics* 107 (2020) 102446.
- [49] J. Wambacq, J. Ulloa, G. Lombaert, S. François, Interior-point methods for the phase-field approach to brittle and ductile fracture, *Computer Methods in Applied Mechanics and Engineering* 375 (2021) 113612.
- [50] J.-Y. Wu, Y. Huang, Comprehensive implementations of phase-field damage models in abaqus, *Theoretical and Applied Fracture Mechanics* 106 (2020) 102440.
- [51] J.-Y. Wu, Y. Huang, V. P. Nguyen, On the bfgs monolithic algorithm for the unified phase field damage theory, *Computer Methods in Applied Mechanics and Engineering* 360 (2020) 112704.
- [52] D. Jodlbauer, U. Langer, T. Wick, Matrix-free multigrid solvers for phase-field fracture problems, *Computer Methods in Applied Mechanics and Engineering* 372 (2020) 113431.
- [53] T. Heister, T. Wick, Parallel solution, adaptivity, computational convergence, and open-source code of 2d and 3d pressurized phase-field fracture problems, *PAMM* 18 (1) (2018) e201800353.
- [54] T. Heister, T. Wick, pfm-cracks: A parallel-adaptive framework for phase-field fracture propagation, *Software Impacts* 6 (2020) 100045.
- [55] D. Arndt, W. Bangerth, B. Blais, T. C. Clevenger, M. Fehling, A. V. Grayver, T. Heister, L. Heltai, M. Kronbichler, M. Maier, et al., The deal. ii library, version 9.2, *Journal of Numerical Mathematics* 1 (ahead-of-print).
- [56] K. Mang, M. Walloth, T. Wick, W. Wollner, Mesh adaptivity for quasi-static phase-field fractures based on a residual-type a posteriori error estimator, *GAMM-Mitteilungen* 43 (1) (2020) e202000003.
- [57] C. Miehe, M. Hofacker, F. Welschinger, A phase field model for rate-independent crack propagation: Robust algorithmic implementation based on operator splits, *Computer Methods in Applied Mechanics and Engineering* 199 (2010) 2765–2778.
- [58] H. Zheng, F. Liu, X. Du, Complementarity problem arising from static growth of multiple cracks and mls-based numerical manifold method, *Computer Methods in Applied Mechanics and Engineering* 295 (2015) 150–171.
- [59] M. Artina, M. Fornasier, S. Micheletti, S. Perotto, Anisotropic mesh adaptation for crack detection in brittle materials, *SIAM Journal on Scientific Computing* 37 (4) (2015) B633–B659.
- [60] A. Kumar, B. Bourdin, G. A. Francfort, O. Lopez-Pamies, Revisiting nucleation in the phase-field approach to brittle fracture, *Journal of the Mechanics and Physics of Solids* (2020) 104027.
- [61] F. Carleo, E. Barbieri, R. Whear, J. Busfield, Limitations of viscoelastic constitutive models for carbon-black reinforced rubber in medium dynamic strains and medium strain rates, *Polymers* 10 (9) (2018) 988.
- [62] J. Plagge, A. Ricker, N. Kröger, P. Wriggers, M. Klüppel, Efficient modeling of filled rubber assuming stress-induced microscopic restructurization, *International Journal of Engineering Science* 151 (2020) 103291.